

4D DAS fiber-coupling effects in freezing near-surface ground conditions

Jihyun Yang^{†*}, Jeffrey Shragge^{†*} and Ge Jin^{*}

[†]Center for Wave Phenomena, ^{*}Department of Geophysics, Colorado School of Mines, Golden CO 80401
email: jihyunyang@mines.edu

ABSTRACT

Distributed acoustic sensing (DAS) increasingly is being used for permanent monitoring in completed downhole installations characterized by near-elastic fiber coupling and high data quality that, for some types of interrogator units (IUs), approaches the particle velocities recorded on single-component geophones. Surface DAS installations, though, tend to be deployed in conduits, in shallow trenches, or even directly on the surface and thus exhibit relatively poorer coupling and lower signal quality for which aggressive filtering is usually required to recover the usable signal. This investigation examines whether near-elastic coupling can be achieved in near-surface horizontal deployments by freezing fiber within shallow trenches thus enabling the use of native velocity acquisition format available on some IUs with only minor, more cosmetic filtering. We report the results of a time-lapse experiment where we acquired DAS data on three 35 m fiber sections deployed at 0 cm, 10 cm and 20 cm depth. Over a six-hour period when the air temperature dropped from +6°C to -6°C we acquired repeat sledgehammer shot records, which clearly exhibit time-varying near-surface and coupling conditions that lead to an observed 4.5% surface-wave velocity increase at colder ground temperatures for data acquired at the 10 cm level compared to those measured at 20 cm depth. We also note significant amplitude brightening in surface-deployed fiber section with decreasing temperatures. Overall, our experiment shows that freezing provides improved - but arguably more complex - fiber-ground coupling and should motivate future cryogenic DAS experiments and increased scrutiny of observed time-lapse variations.

Key words: Interrogator Design, Coupling, DAS, Velocity, Strain-rate

1 INTRODUCTION

The use of distributed acoustic sensing (DAS) in permanent monitoring installations is increasingly being used in industry for time-lapse (4D) seismic investigations (Mateeva et al., 2017; Pevzner et al., 2020; Wang et al., 2020; Zhu et al., 2021). Downhole fiber installations often can achieve near-perfect elastic coupling with the surrounding earth (e.g., grouting a fiber to the outside of the casing) and can acquire high-quality data that can approach the angular response of single-component geophones for some interrogator units (IUs). For lower-cost surface fiber deployments (e.g., fiber directly laid on the ground, passed through buried conduits, or trenched up to 1.5 m depth), though, it is less obvious how such elastic coupling can be achieved. Moreover, for imperfect coupling scenarios, an interesting question is how deleterious are the effects of spatially and diurnally variations in the fiber-ground coupling conditions on DAS recordings.

Despite the complexities involved in horizontal fiber installations, including ground-fiber coupling, numerous DAS success stories have emerged in the literature. One class of examples uses pre-existing (telecommunication) surface deployments (i.e., so-called dark fiber), which enables ubiquitous recording on a previously established array. For example, Fernández-Ruiz et al. (2020) show the promising performance of low-frequency (1-120 s period) DAS recording when compared to high-quality broadband seismometers. Becker and Coleman (2019) present a laboratory experiment that demonstrates the possibility of DAS-based earth-tide observations. Williams et al. (2019) and Sladen et al. (2019) report successfully detecting ocean microseisms and regional

earthquakes using ocean-bottom fiber arrays with onshore DAS IUs. Finally, Lindsey et al. (2020) analyze and calibrate the DAS instrument response, especially for periods greater than 1 s, using co-located broadband seismometer as the reference of true ground motion. They stress that the DAS instrument response should be evaluated as a single system, including optical interferometry setup, fiber type, and conduit coupling, and point out that the IU design can influence the recording format and optical correlation characteristics.

Most DAS IU designs measure the strain/strain rate using a gauge length defined either in hardware or via post-processing. An alternative approach possible with the Terra15 Treble IU (Issa et al., 2018) is to record DAS data in a “velocity” format $v(x, t)$ that is the integral of the strain rate $\dot{\epsilon}$ from the interrogation point (at $u = 0$) along the fiber to point $u = x$

$$v(x, t) = \int_0^x \dot{\epsilon}(u, t) du, \quad (1)$$

where t is time and u is an integration variable. Under perfect elastic coupling conditions, the recorded quantity is proportional to particle velocity as measured on a single-component geophone aligned with the fiber direction. Using a completed downhole fiber installation, Sidenko et al. (2020) show that DAS data acquired in the Terra 15 Treble velocity format exhibit a near-equivalence to the ground motion recorded on a co-located borehole geophone array. This means that this acquisition mode with an elastically coupled fiber can achieve a geophone-like $\cos \theta$ sensitivity pattern (where θ is the incidence angle) compared to conventional $\cos^2 \theta$ relationship of strain-rate DAS measurement (Benioff, 1935; Kuvshinov, 2016). Importantly, no post-processing first-derivative filtering was necessary for Sidenko et al. (2020) to recover high-quality DAS signals in the velocity format, which forestalled introducing the associated adverse filtering effects (e.g., spectral notches, downweighting of low-wavenumber components) commonly present in DAS strain-rate observations. However, we stress that imperfect mechanical coupling will result in low-wavenumber noise that accumulates along the fiber and must be handled through post-acquisition filtering.

In this study, we investigate whether the advantages of using a Treble IU in native velocity format can be achieved for a surface fiber installation. With the aim of achieving a scenario approaching near-elastic coupling, we describe a small-scale investigation where we deploy three segments of a 125 m fiber in a shallow trench in the frozen earth that was watered down and left to freeze in the ground overnight. Over the following day, we acquired repeat sledgehammer shots as the outside air temperature reached 6.5°C mid-afternoon and then fell to -6.5°C by mid-evening. The temperature drop allowed us to investigate the benefits of acquiring DAS velocity data on a near elastically coupled surface fiber array as well any possible time-varying coupling effects due to diurnal temperature variations about the freezing point. We begin by describing the experimental methodology including the experimental setup, the raw data results, and the data-processing strategy we apply to handle the residual fiber-ground coupling effects. We then present processed shot-gathers and the observed time-lapse (4D) amplitude and velocity variations associated with diurnal variations in fiber-ground coupling. We conclude by discussing the implications for 4D DAS analyses in cryoseismic investigations.

2 METHODOLOGY

To investigate the effects of freezing and thawing on fiber-ground coupling, we selected suitable test dates (15 and 16 February 2021) where the forecast for Arvada, CO where the test took place predicted the air temperature would remain well below the freezing point on the first day, rise above 0°C by mid-morning on the second day, reach 6°C by mid-afternoon, and then return to below freezing by the early evening after the 5:38 PM sunset.

To set up the fiber acquisition geometry, we first trenched one 35 m section of fiber into the ground at approximately 20 cm depth (Section A), covered it with compacted soil, and then thoroughly watered it down. We then looped the fiber back along the same trench at approximately 10 cm depth (Section B), again covering the fiber, compacting the soil and watering it down. Finally, we ran the remaining fiber directly on the surface (Section C). Figure 1 depicts the installed fiber a few minutes after watering down the section. The three sections allowed us to compare the elastic coupling environments at different depths with variable sensitivity to the diurnal freeze-thaw cycles. Figure 2 shows the overall fiber deployment geometry with the following points: (1) the interrogator is housed in a garage at point ① at 0 m distance; (2) the source point is located ① at 20 m; (3) Section A runs between 20-55 m up to the turnaround point at ②; (4) Section B runs between 55-90 m up to the turnaround point at ③; and (5) Section C runs between 90-120 m up to the end of the fiber at ④. For comparison purposes, we installed vertical component geophones 30 cm from the fiber (Figure 1) for use in later analysis.

The DAS IU used for the seismic acquisition was a circa mid-2020 Treble IU provided by Terra15 Technologies Pty Ltd of Perth, Australia. The phase-based system has a proprietary design that is optically designed to eliminate amplitude and polarization fading (Issa et al., 2018). The Treble IU is capable of acquiring DAS seismic data either as native velocity or in a strain-rate format with the gauge length (GL) modifiable through post-processing.

We acquired 3 Tb of DAS data in continuous mode over the two-day experiment in the native velocity format at 0.038 ms and



Figure 1. Fiber on Section B with the deployed geophones to the left. The steam is from hot water poured on the ground to eventually freeze the fiber to improve ground-fiber coupling. (Photo credit: Iga Pawelec)

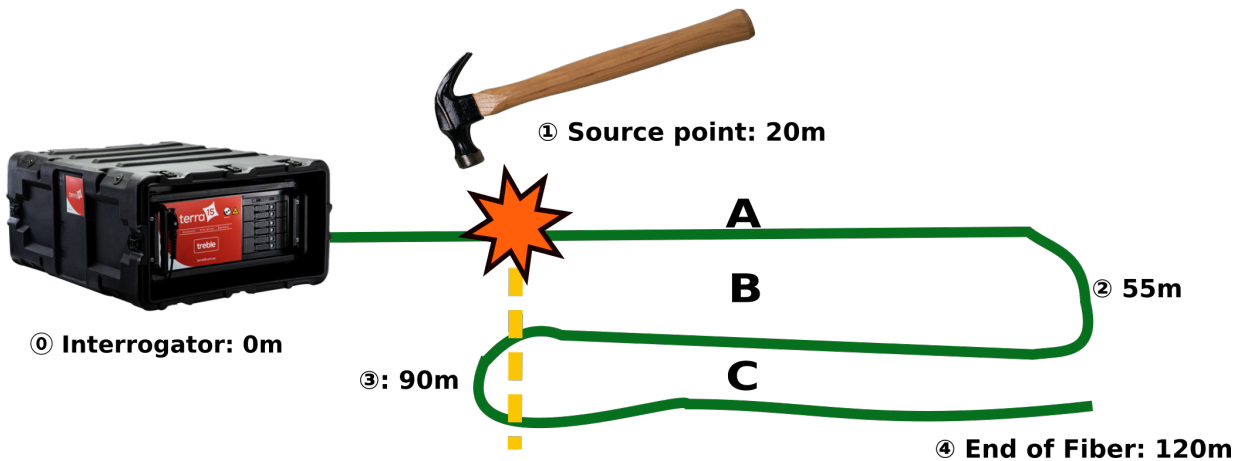


Figure 2. Schematic drawing of DAS acquisition geometry. Sections A and B correspond to the trenched fiber locations, where the former has a deeper trenching depth (approx. 20 cm) than the latter (approx. 10 cm). The fiber in Section C is laid on top of the ground. Sections A-C are at 20-55 m, 55-90 m and 90-120 m in the fiber layout, respectively.

0.8 m temporal and spatial sampling intervals, respectively. To test the spatio-temporal variations in the fiber-ground coupling, we used a sledgehammer and metal plate as an energy source and generated shots at approximately 30-minute intervals for 12 hours from 9:00 AM to 9:00 PM. As shown in Figure 1, the three effective shot locations as observed on Sections A-C are 20 m, 90 m (back up the fiber), and 90 m (down the fiber) from the IU, respectively. The first processing step involved window selection where we used the noted shot times to extract one-minute data streams of approximately 1 Gb size. Because the frequencies of interest from the sledgehammer shots were lower than 150 Hz, we low-passed filtered with a 150 Hz cutoff and then decimated the data set to a more reasonable size. We then corrected the polarity of the data acquired Section B to compensate for the reversed fiber orientation (see Figure 1).

Figure 3a presents a shot gather recorded at 9:00 PM in the native velocity format. The arrivals are clearly identifiable in all three fiber sections. Although horizontal arrivals are present, the moveouts are too fast to be related to a passing seismic wave disturbance and thus likely represent a coherent noise source related to vibrations induced within the IU due to sledgehammering at too close of a distance. Figure 3b corresponds to a frequency-wavenumber ($f - k$) spectra of the shot gather shown in Figure 3a. The identified noise source maps to the strong low-wavenumber components observed as two lobes with between 20-60 Hz as well as the vertical “washboard” pattern.

The usual processing step (though not necessarily required for this data set) would be to obtain strain-rate data from the native velocity measurement by applying some variation of a spatial first-derivative operator. To illustrate the effects of doing so, we examine two different first-derivative filtering operations. The first is to apply a GL filter of length L_G through

$$\varepsilon'_E(x, t|L_G) \approx \frac{v(x + L_G/2, t) - v(x - L_G/2, t)}{L_G}, \quad (2)$$

where ε'_E is the estimated along-fiber strain rate. The second approach uses a 12th-order Taylor-series finite-difference (FD) approximation of the first-derivative operator

$$\varepsilon'_E(x, t|c_k) \approx \frac{1}{\Delta x} \sum_{k=1}^6 c_k (v(x + k\Delta x, t) - v(x - k\Delta x, t)), \quad (3)$$

where $c_k = [23760, -7425, 2200, -495, -72, 5]/27720$ are the corresponding FD coefficients, and Δx is the spatial sampling interval along the fiber. The left and right columns of Figure 4 presents three different FIR (finite impulse response) filters along with their associated spectral responses. Overall, we observe that the different filtering approximations lead to very different strain-rate approximations. In particular, a shorter GL introduces stronger long-wavelength filtering (Figure 4a and 4b), while a longer GL induces additional spectral notches (Figure 4c and 4d). Conversely, the 12th-order spatial derivative does not introduce the notches save for at the DC component (Figure 4e and 4f), but clearly imparts the expected $|k|$ weighting that sees a linear increase at higher wavenumbers until reaching the approximation limit close to the Nyquist wavenumber.

To illustrate the denoising benefits of using a first-derivative filter to obtain a strain-rate panel estimate, we apply the gauge-length filter approach in equation 2 with $L_G = 0.8 = \Delta x$ m, equivalent to the spatial sampling interval. Figure 3c presents the filtered results of the velocity data from Figure 3a, while Figure 3d shows the associated filtered $f - k$ spectrum. The low-order 1D spatial-derivative filter acts as a low-cut filter that through the conversion to strain rate removes the strong low-wavenumber noise in Figure 3b, but also significantly upweights the noise at high wavenumbers. To evaluate the effects of the strain-rate transformation of different gauge lengths on a single section, we first window out data in Section A and generate four $f - k$ spectra. Figure 5a-5c show the raw velocity data, for $L_G = 6.4$ m (corresponding to the filter in Figure 4a) and for $L_G = 11.2$ m (corresponding to the filter in Figure 4c). The raw velocity $f - k$ panel has the strongest near-DC component, while the $L_G = 11.2$ m example largely preserves low frequencies post-filtering, though the filtering operation has clearly introduced notches that adversely affect the observed $f - k$ spectrum. Figure 5d presents the $f - k$ spectra after applying the 12th-order first-derivative filter shown in Figure 4e and 4f.

Although the first-derivative strain-rate calculation is by now a standard technique, we point out that applying a standard frequency-domain velocity dip filter used for decades in seismic data processing may be a better approach for removing the coherent noise observed in Figure 3a. A velocity dip filter (also known as a fan filter) is straightforward to implement, has few tunable parameters, and leads to high-quality filtered output when the signal and noise dip spectra are clearly separated like they are in this data set. Following such an approach allows for the resulting panel to be considered as “filtered-velocity” panel rather than a “strain-rate” panel. Figure 3e and 3f illustrate the benefits of applying the dip-filter approach to this data set. The fan-like pattern observed in the $f - k$ spectra, corresponding to a pass band for waves travelling horizontally at velocities between ± 100 m/s and 1800 m/s, has removed the near-zero wavenumber energy noise without introducing notches or significant upweighting of high-wavenumber components. Thus, velocity-dip filtering represents our preferred approach for this data set, though we point out that this approach becomes less useful as one moves away from a nearly elastically coupled fiber-ground system.

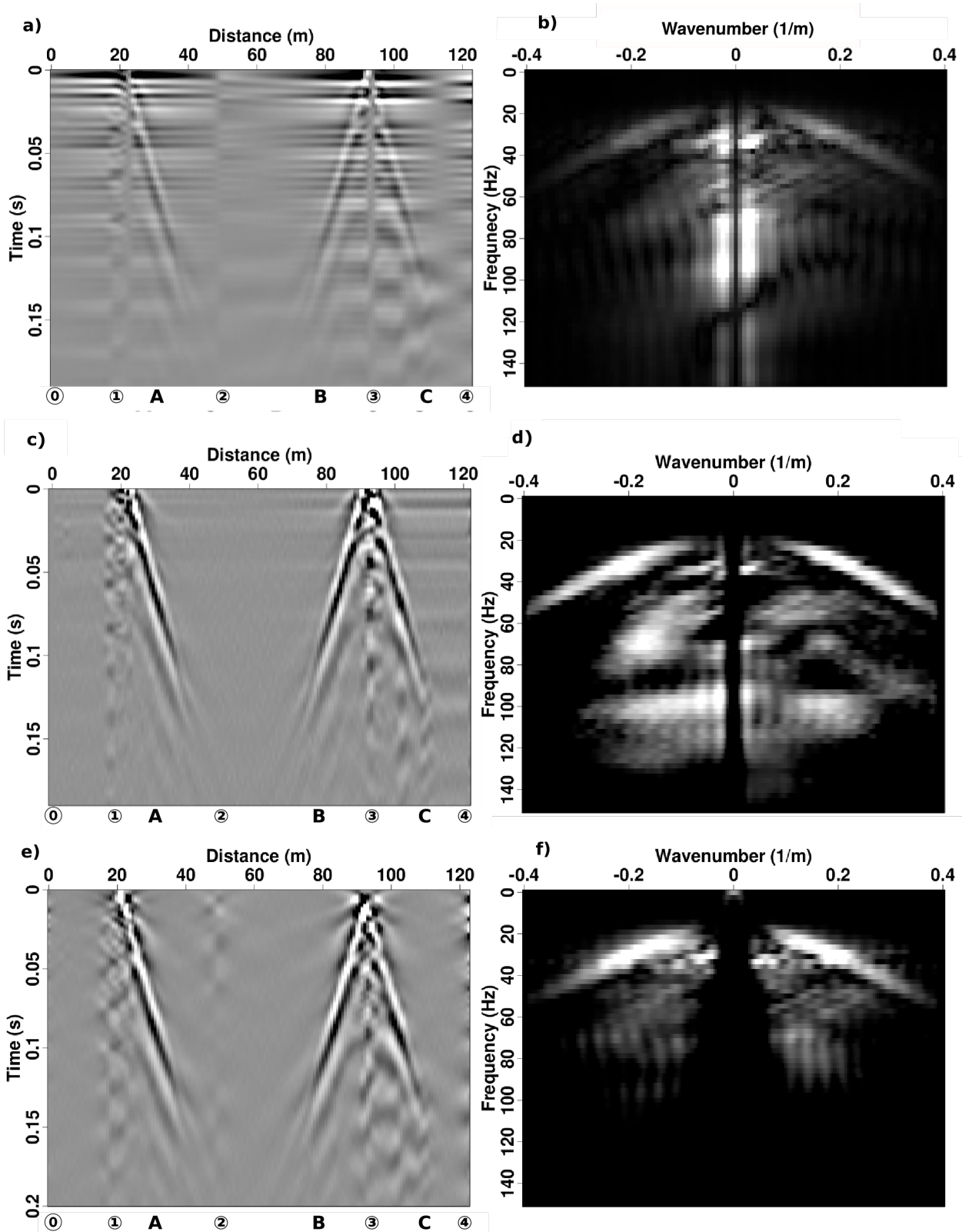


Figure 3. (a) Velocity data for a hammer shot recorded at 8 PM after polarity correction applied to Section B. Note that the record is contaminated with horizontal noise that has a moveout too fast to be a seismic event and is thus likely associated with hammering too close to the IU. (b) The associated frequency-wavenumber $f - k$ plot where the vertical “washboard” striping is due to the presence of the horizontal noise observed in (a). (c) Strain-rate data for the same shot in (a) after applying gauge length $L_G=0.8$ m. (d) $f - k$ spectra of the filtered shot record shown in (c). (e) Dip-filtered velocity data for the same shot in (a). (f) The $f - k$ spectra for the filtered shot record shown in (e).

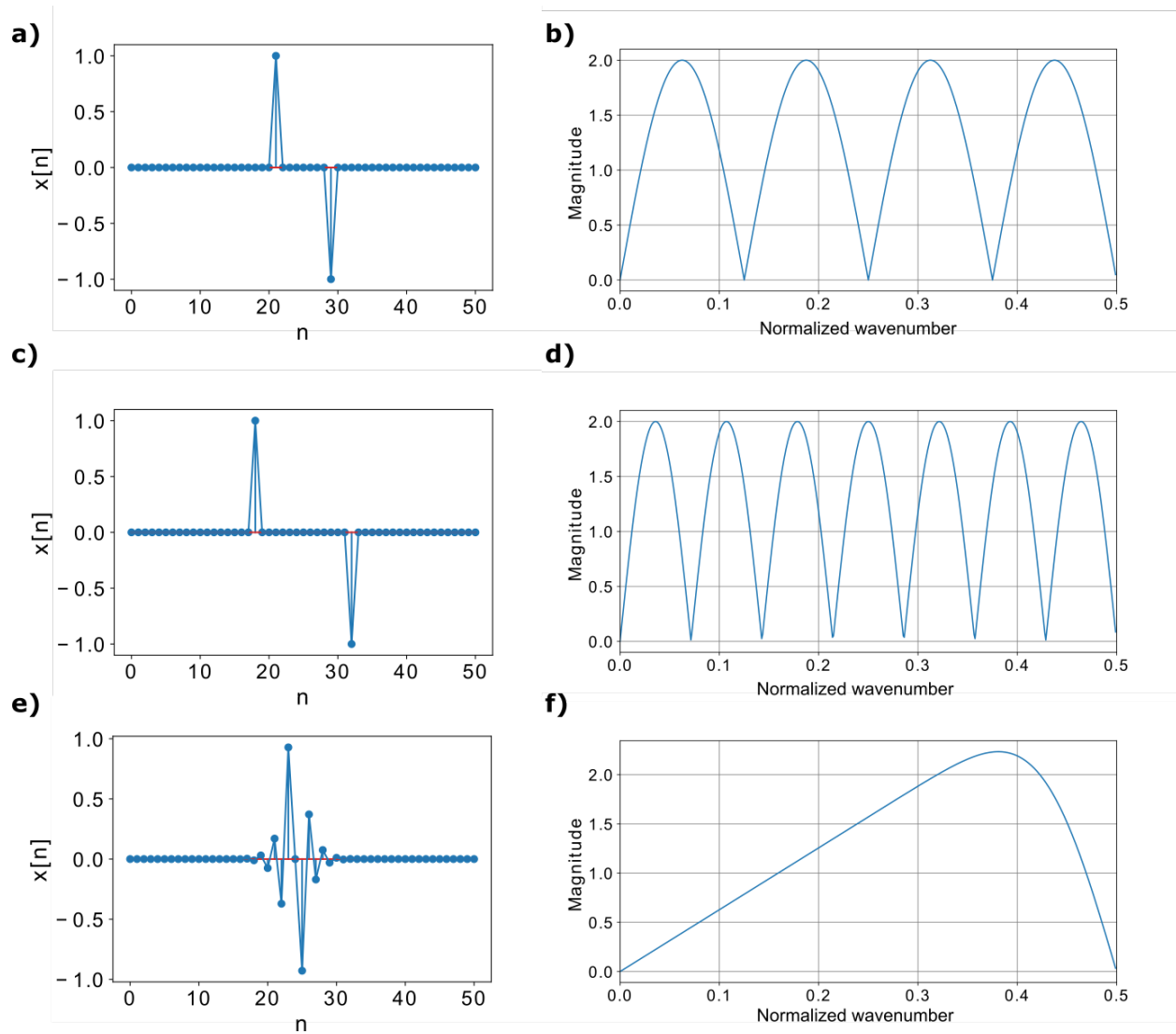


Figure 4. Three FIR filters first-derivative approximations and their associated magnitude spectra. (a) $L_G = 8$ unit filter. (b) Magnitude spectrum of (a). (c) $L_G = 14$ unit filter. (d) Magnitude spectrum of (c). (e) 12th-order FD first-derivative approximation. (f) Magnitude spectrum of (e).

3 RESULTS

Having specified our preferred approach for filtering the observed shot-gather data, we now turn to the time-lapse nature of the experiment and investigate how the characteristics of the repeat shot gathers change with the varying environmental conditions. Figure 6a and 6b present a series of three shot gathers acquired at 3:00 PM, 5:30 PM, and 9:00 PM respectively recorded on Section A at 20 cm depth and Section C lying on the surface. We applied a consistent velocity-dip filter to each panel to remove any horizontal artifacts similar to those observed in Figure 3a. The shot gathers recorded on Section A show consistent amplitudes during the six-hour recording period. Conversely, the shot gathers recorded on Section C exhibit increasing surface-wave amplitudes over the same recording time, which are most likely caused by improved fiber-ground coupling due to the changing near-surface conditions induced by the thaw-freeze cycle. In particular, we expect soil conditions at the surface to hardened as the temperature drops below freezing post-sunset due to the formation of ice on the fiber and in the compacted soil.

Having observed a significant temperature dependence on surface coupling, we investigate whether the data show any evidence for 4D near-surface velocity variations. Because obtaining a consistent time zero is challenging for hammer-source data, we first optimally align the surface-wave arrivals recorded at 15 m source-receiver offset on Section A using the multi-channel cross-correlation (MCCC) approach of VanDecar and Crosson (1990). This approach, originally developed for determining the relative

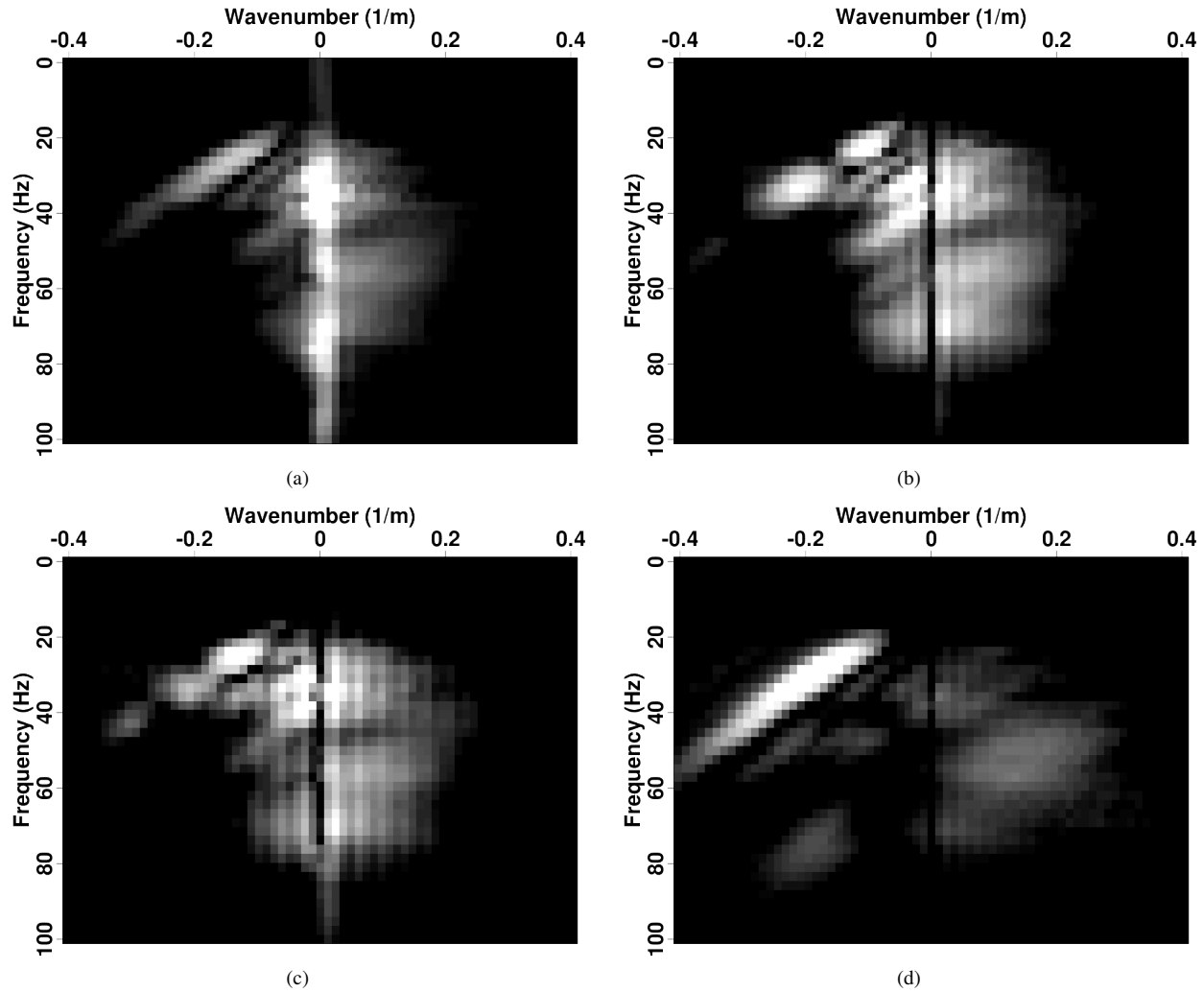


Figure 5. $f - k$ spectra for a shot gather recorded on Section A. (a) Raw velocity data. (b) Strain-rate data with $L_G = 6.4$ m (corresponding to the filter in Figure 4a). (c) Strain-rate data with $L_G = 11.2$ m (corresponding to the filter in Figure 4c). (d) Strain-rate data after applying 12th-order Taylor-series first-derivative filter as shown in Figure 4e.

phase arrival times and uncertainty estimates for teleseismic events, can be used to calibrate an optimal set (i.e., in a least-squares sense) of alignment times for any batch of waveform data. The algorithm derives relative delay times based on the maximum correlation value between all possible pairs of traces. The computed delay times lead to an overdetermined set of linear equations whose solutions are a set of optimal relative zero-mean traveltimes for optimal alignment.

Here, we extract a trace from ten shot gathers at a fixed 15 m source-receiver offset, which we use to form the set of linear equations for MCCC analysis. We solve the MCCC system of equations using a standard least-squares approximation to obtain an optimal set of shot static corrections, which we apply to individual data panel (i.e., a constant shift for Sections A-C). Figure 7a and 7b presents the 15 m source-receiver traces after applying the MCCC-derived shot statics for Sections A and B, respectively. On Section A, we observe that the arrivals between approximately 0.04 s and 0.05 s are now fairly flat between shots 5 and 15; however, the arrivals on Section B drift upward with increasing shot index number indicating an increasing near-surface surface-wave velocity.

We attribute these variations to a relative velocity increase in the (partially) frozen soil of the mid-layer. To better quantify the noted 4D variations, we calculate and average the velocities of ten shots recorded at five times between 3:00 PM and 9:00 PM. Figure 8 presents the relative slowness (i.e., reciprocal of velocity) results as green dots with associated error bars along with the recorded air temperature shows as red stars. These observations show a 4.5% increase in the near-surface surface-wave velocity as

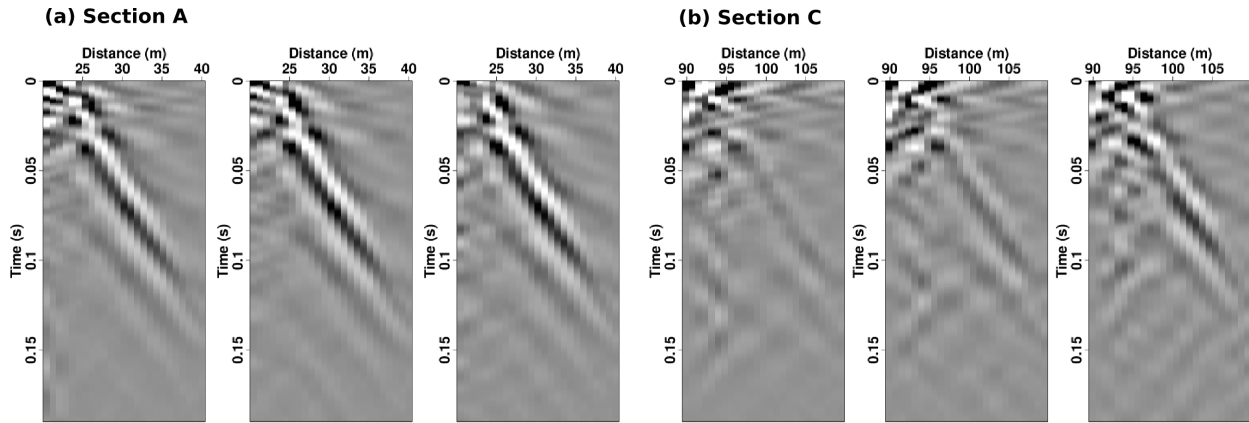


Figure 6. Recorded shot-gather velocity data acquired at 3:00 PM (air temp. +2.5°C), 5:30 PM (air temp. -0.5°C) and 9:00 PM (air temp. -6.5°C). (a) Section A at 20 cm trenching depth. (b) Section C lying on the surface.

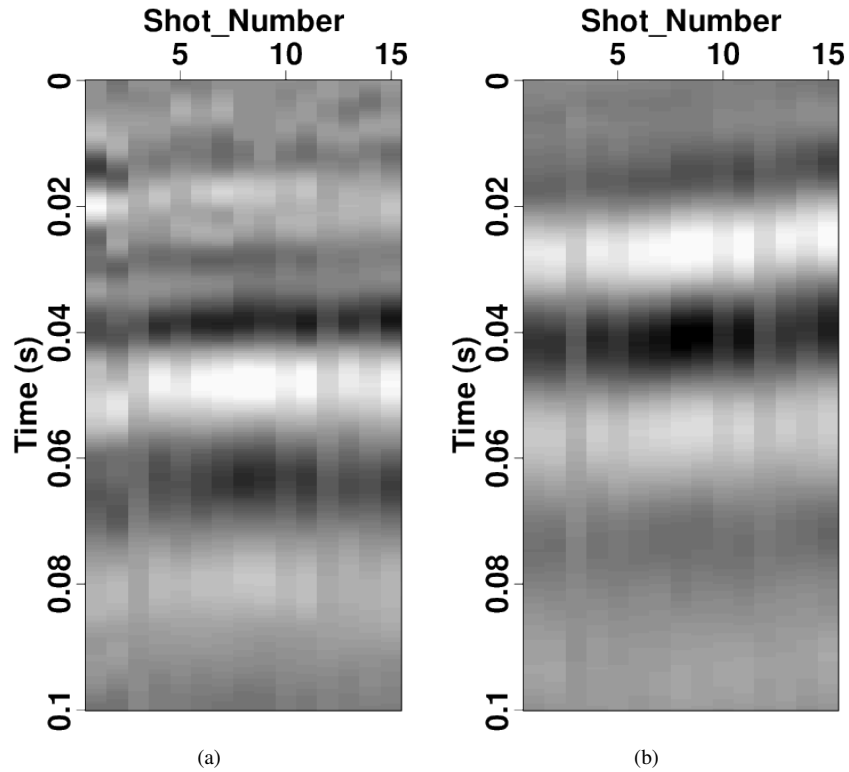


Figure 7. (a) Calibrated shot gather arrivals at 15 m source-receiver offset recorded on Section A after applying the MCCC algorithm to optimally time-zero corrections of the hammer shots. (b) The moveout results on Section B after applying the same time-zero corrections as in (a). The positive slope with increasing shot index number indicates increasing surface-wave velocities due to the freezing of soil moisture in the near surface.

temperature drops below 0° , the sun sets, and ground freezing commences. We note that while the highlighted trend appears linear, this does not imply that there is a causal linear relationship between surface-wave velocity and air temperature.

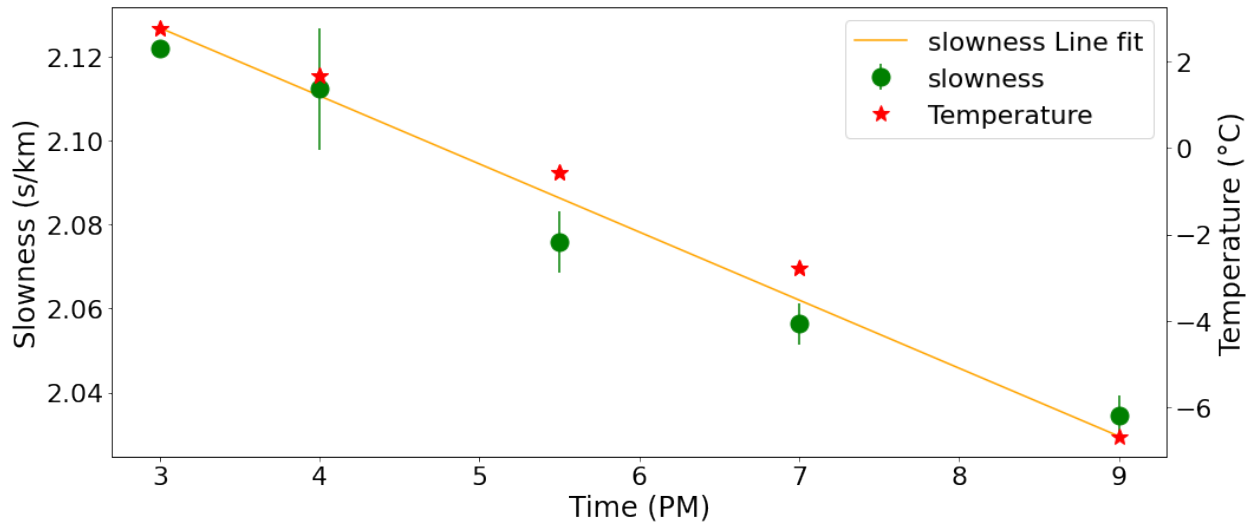


Figure 8. Measured ground velocity for Section B (green dots), the best-fitting line (yellow) and the recorded air temperature (red stars) in Arvada, CO on 16 February 2021. Error bars are indicated for the velocity estimates. Note that while the highlighted trend appears linear, this does not imply that there is a causal linear relationship between surface-wave velocity and air temperature.

4 DISCUSSION

The velocity changes noted in Section B relative to Sections A and C open up a number of interesting questions. We attribute the velocity difference results noted in Section B to the combined influences of cooling air and colder ground temperatures. While a more thorough investigation involving ground-temperature measurements is warranted, the noted surface-wave velocity variations suggest a hitherto unconsidered aspect of DAS monitoring in horizontal fiber installations. In particular, one needs to be careful when attributing the genesis of 4D surface-wave velocity variations in a near-surface environment susceptible to freeze-thaw cycles. However, this 4D effect likely can be mitigated with an increased trenching depth, though the overlying thermal-induced variations may not be insignificant. Further investigations are needed to set up optimal deployment depth and temperature that best ensures 4D repeatability of the entire DAS sensing network. For example, deploying fiber at the frozen lake and monitoring changes for the freezing-thawing cycle would provide another example of how temperature and fiber coupling affect the DAS data. Booth et al. (2020) show the potential for cryoseismic VSP DAS data by detecting anisotropy at 150 m depth of the glacier. To further investigate the potential of cryogenic DAS installation, horizontal fiber deployments on a frozen lake surface represents a related and potentially interesting test case.

5 CONCLUSIONS

We present an experiment that evaluates the Treble 15 native DAS velocity format recorded on fiber deployed at variable trenching depths, soil conditions, and diurnal coupling effects. We observe that the freeze-thaw cycle in the near-surface soil alters the coupling of the fiber during the day, which is most evident in shallow (10 cm) trench data and ground exposed to open air. The trenched fiber in frozen soil provides sufficient coupling to record the native velocity format DAS data throughout the day (with minor dip-filter processing). However, fiber simply laid on the ground shows poor quality overall, except for later times (7:00-9:00 PM) when the temperature drops and the fiber becomes better coupled to the ground likely through partial freezing. Our result suggests freezing and trenching provide good fiber-ground coupling for recording in native velocity format, which encourages future cryogenic DAS experiments such as installation on frozen lakes, glaciers and snowpack.

6 ACKNOWLEDGEMENTS

We thank the sponsors of the Center for Wave Phenomena (CWP), whose support made this research possible. We thank Aaron Girard and Iga Pawelec (CSM) for help on this experiment, and Nader Issa and Michael Roelens (Terra15) for useful technical suggestions. The reproducible numerical examples and plots use the Madagascar software package (<http://www.ahay.org>).

REFERENCES

- Becker, M. W., and T. I. Coleman, 2019, Distributed acoustic sensing of strain at earth tide frequencies: *Sensors*, **19**, 1975.
- Benioff, H., 1935, A linear strain seismograph: *Bulletin of the Seismological Society of America*, **25**, 283–309.
- Booth, A., P. Christoffersen, C. Schoonman, A. Clarke, B. Hubbard, R. Law, S. Doyle, T. Chudley, and A. Chalari, 2020, Detecting anisotropy using distributed acoustic sensing and fibre-optic seismology in a fast-flowing glacier in greenland, *in* EGU General Assembly 2020: EGU General Assembly, 7709.
- Fernández-Ruiz, M. R., M. A. Soto, E. F. Williams, S. Martin-Lopez, Z. Zhan, M. Gonzalez-Herraez, and H. F. Martins, 2020, Distributed acoustic sensing for seismic activity monitoring: *APL Photonics*, **5**, 030901.
- Issa, N., M. Roelens, and S. Frisken, 2018, Distributed optical sensing systems and methods: PCT Patent Application PCT/AU2018/050775.
- Kuvshinov, B., 2016, Interaction of helically wound fibre-optic cables with plane seismic waves: *Geophysical Prospecting*, **64**, 671–688.
- Lindsey, N. J., H. Rademacher, and J. B. Ajo-Franklin, 2020, On the broadband instrument response of fiber-optic DAS arrays: *Journal of Geophysical Research: Solid Earth*, **125**, e2019JB018145.
- Mateeva, A., J. Lopez, D. Chalenski, M. Tatanova, P. Zwartjes, Z. Yang, S. Bakku, K. De Vos, and H. Potters, 2017, 4D DAS VSP as a tool for frequent seismic monitoring in deep water: *The Leading Edge*, **36**, 995–1000.
- Pevzner, R., B. Gurevich, A. Pirogova, K. Tertyshnikov, and S. Glubokovskikh, 2020, Repeat well logging using earthquake wave amplitudes measured by distributed acoustic sensors: *The Leading Edge*, **39**, 513–517.
- Sidenko, E., A. Bona, R. Pevzner, N. Issa, and K. Tertyshnikov, 2020, Influence of Interrogators' Design on DAS Directional Sensitivity: *EAGE*, 1–5.
- Sladen, A., D. Rivet, J.-P. Ampuero, L. De Barros, Y. Hello, G. Calbris, and P. Lamare, 2019, Distributed sensing of earthquakes and ocean-solid earth interactions on seafloor telecom cables: *Nature Communications*, **10**, 1–8.
- VanDecar, J., and R. Crosson, 1990, Determination of teleseismic relative phase arrival times using multi-channel cross-correlation and least squares: *Bulletin of the Seismological Society of America*, **80**, 150–169.
- Wang, Z., B. Lu, Q. Ye, and H. Cai, 2020, Recent Progress in Distributed Fiber Acoustic Sensing with Φ -OTDR: *Sensors*, **20**, 6594.
- Williams, E. F., M. R. Fernández-Ruiz, R. Magalhaes, R. Vanthillo, Z. Zhan, M. González-Herráez, and H. F. Martins, 2019, Distributed sensing of microseisms and teleseisms with submarine dark fibers: *Nature Communications*, **10**, 1–11.
- Zhu, T., J. Shen, and E. R. Martin, 2021, Sensing Earth and environment dynamics by telecommunication fiber-optic sensors: an urban experiment in Pennsylvania, USA: *Journal of Geophysical Research: Solid Earth*, **12**, 219–235.